

RESEARCH ARTICLE

10.1002/2016JA023427

Key Points:

- Radar, optical, and satellite observations of equatorward propagating auroral arcs driven by ULF waves
- The auroral arcs are signatures of a FLR driven by an interaction with a compressional fast mode wave propagating earthward from the tail
- The wave energy is dissipated through ionospheric Joule and/or ion frictional heating and auroral particle acceleration

Correspondence to:

L. J. Baddeley,
lisa.baddeley@unis.no

Citation:

Baddeley, L. J., D. A. Lorentzen, N. Partamies, M. Denig, V. A. Pilipenko, K. Oksavik, X. Chen, and Y. Zhang (2017), Equatorward propagating auroral arcs driven by ULF wave activity: Multipoint ground- and space-based observations in the dusk sector auroral oval, *J. Geophys. Res. Space Physics*, 122, 5591–5605, doi:10.1002/2016JA023427.

Received 2 SEP 2016

Accepted 24 APR 2017

Accepted article online 26 APR 2017

Published online 9 MAY 2017

Equatorward propagating auroral arcs driven by ULF wave activity: Multipoint ground- and space-based observations in the dusk sector auroral oval

L. J. Baddeley^{1,2,3} , D. A. Lorentzen^{1,2,3} , N. Partamies^{1,2} , M. Denig⁴ , V. A. Pilipenko⁵ , K. Oksavik^{1,2} , X. Chen^{1,2,6} , and Y. Zhang⁷ 

¹Department of Geophysics, University Centre in Svalbard, Longyearbyen, Norway, ²Birkeland Centre for Space Science, Department of Physics and Technology, University of Bergen, Bergen, Norway, ³British Antarctic Survey, Cambridge, UK, ⁴National Centers for Environmental Information, Boulder, Colorado, USA, ⁵Institute of Physics of the Earth, Moscow, Russia, ⁶SOA Key Laboratory for Polar Science, Polar Research Institute of China, Shanghai, China, ⁷The Johns Hopkins University Applied Physics Laboratory, Laurel, Maryland, USA

Abstract Observations of multiple equatorward propagating arcs driven by a resonant Alfvén wave on closed field lines are presented. Data sets from the European Incoherent Scatter Svalbard Radar (ESR) and Meridian Scanning Photometer in Longyearbyen, All-Sky Camera in Ny Ålesund, ground magnetometer data in Svalbard, and Defense Meteorological Satellite Program (DMSP) F16 satellite were utilized to study the arc structures. The arcs had an equatorward phase propagation of $\sim 0.46 \text{ km s}^{-1}$ and were observed in the dusk ionosphere from 1800 to 2030 magnetic local time. Analysis of the optical data indicates that the Alfvén wave had a frequency of 1.63 mHz and an azimuthal wave number, $m \sim -20$ (the negative sign indicating a westward propagation). Inverted-V electron populations associated with field-aligned currents of between 0.5 and $0.8 \mu\text{A m}^{-2}$ are observed by DMSP F16 inside the arc structures. In addition to electron density enhancements associated with the arcs, the ESR data show elevated ion temperatures in between the arcs consistent with electric field enhancements and ionospheric heating effects. The combination of ESR and DMSP F16 data indicates that the wave energy was dissipated through ionospheric Joule and/or ion frictional heating and acceleration of particles into the ionosphere, generating the auroral displays. The fine-scale structuring, in addition to the propagation direction and scale size, would suggest that the auroral features are the signatures of a field line resonance driven by an interaction with a compressional fast mode wave propagating earthward from the magnetotail.

1. Introduction

Ultralow frequency (ULF) magnetohydrodynamic (MHD) waves play a vital role in the transfer of energy and momentum throughout the Solar Wind-magnetospheric-ionospheric system. Shear Alfvén waves can form standing mode structures on the Earth's magnetic field lines, with the wave Poynting vector directed along the magnetic field and the ionosphere considered as the reflecting boundary. Here the foot points of the field lines in the ionosphere can then be considered as either nodes or antinodes. The standing wave structures have velocity, magnetic field, and electric field perturbations perpendicular to the magnetic field line (i.e., either radially or azimuthally directed in the magnetospheric equatorial plane) with the electric field perturbations rotated through 90° from the magnetic and velocity perturbations. Toroidally polarized waves have magnetic field oscillations confined in the azimuthal direction (and the resulting electric field oscillations in the radial direction), while poloidally polarized waves have the magnetic field oscillations confined in a radial direction (and the resulting electric field oscillations in the azimuthal direction). Toroidal mode waves are traditionally thought of as having large azimuthal scale size (or low m , where m is the effective azimuthal wave number assuming the wave structure has a dependence in azimuth, φ , of $e^{im\varphi}$) and are termed field line resonances (FLRs) [see Wright and Mann, 2006, and references therein]. They have an energy source in the form of a fast mode compressional wave which undergoes a mode conversion to a Shear Alfvén mode on a geomagnetic field line with a matching eigenfrequency. Subsequent to this mode conversion, the wave energy is then primarily lost through Joule heating or some collisionless dissipation mechanisms [e.g., Newton et al., 1978] at the ionospheric footprint of the field line. The most often cited generation mechanisms for the fast mode waves in the flanks and dayside magnetosphere are external to the Earth's magnetosphere, in the form of Kelvin-Helmholtz instability (KHI) on the magnetospheric flanks or sudden Solar Wind pressure pulses (SWPP) at

the magnetopause [see *Mann and Wright, 1999*, and references therein]. In the tail region, a reconfiguration of the magnetic field (such as that caused by a substorm) has been considered as an internal driver of fast mode compressional waves [e.g., *Zheng et al., 2006*]. The azimuthal propagation of the FLR is also related to the generation mechanism giving rise to either an antisunward (e.g., KHI or SWPP generated) or sunward (e.g., substorm generated) propagation direction. Poloidal mode standing wave structures are generally thought to have an energy source internal to the Earth's magnetosphere in the form of energetic particle populations injected into the magnetosphere from the tail. Subsequent to this injection, ions propagate along drift paths in a westward direction and electrons in an eastward direction. The resulting wave propagation direction would thus depend on the interacting driving particle population, and there are several theories detailing such mechanisms [e.g., *Southwood and Hughes, 1983; Chen and Hasegawa, 1991; Mager and Klimushkin, 2008*]. They generally have smaller azimuthal scale sizes than toroidal mode waves (the exception being so called "Giant Pulsations" which generally have m numbers of between -20 and -40) [e.g., *Chisham et al., 1997*].

FLRs in the Pc5 range (period 150–600 s) have been observed to modulate auroral structures into discrete periodic arcs in the dawn, dusk, and midnight sector ionosphere [e.g., *Samson et al., 1996; Rae et al., 2005*]. In such cases the FLR carries strong field-aligned currents (FACs) with densities up to several $\mu\text{A m}^{-2}$ into and out of the ionosphere. Inside the arcs, intense upward FACs are associated with downward going electron populations which have been accelerated through a parallel electric field, E_{\parallel} [e.g., *Wright et al., 2003*]. This represents an energy sink for the FLR in addition to ionospheric Joule heating at the foot of the field line.

In the case of auroral arcs related to externally driven FLRs a common feature is a poleward phase propagation of the arcs when observed in meridian scanning photometer (MSP) and ALL-SKY Camera (ASC) data. This can be understood in terms of the sign of the radial gradient of the Alfvén field line period. Typically, in the region of the magnetosphere, which maps to auroral latitudes, the Alfvén period increases with L shell, resulting in an apparent poleward propagation of any ground response.

Colocated ground-based magnetometer data also show evidence of wave activity associated with large amplitude FLRs. The ionosphere modifies the magnetospheric ULF wave signature, which causes a rotation of the magnetic signature of the wave as detected on the ground [e.g., *Hughes, 1983*]; thus, for a FLR with radial magnetic perturbations in the magnetospheric equatorial plane the largest perturbations will be observed in the north-south (meridional) component of ground magnetometer data. Additionally, an amplitude peak in the observed wave power at the resonant frequency accompanied by a 180° phase change as a function of latitude across this resonant peak (with a poleward phase propagation) is also observed. Both are well-known characteristic of FLRs [Walker et al., 1979].

Observations of equatorward propagating auroral structures associated with FLRs are much rarer [Rae et al., 2014; Mathews et al., 2004]. In both cases the authors cite an internal generation mechanism in the form of either coupling with a compressional mode generated in the magnetotail or drifting particle populations. The event presented here will be discussed in relation to these two previous events in section 3 of this paper.

This paper presents the first observations of ULF wave-driven equatorward propagating auroral arcs utilizing direct measurements of ionospheric temperature and density enhancements (European Incoherent Scatter (EISCAT) Svalbard radar), auroral structuring (Meridian Scanning Photometer and All Sky camera), and auroral particle precipitation (Defense Meteorological Satellite Program (DMSP) F16 satellite).

2. Data Presentation

The observations occurred on 27 December 2007 between 1530 and 1730 UT. Conditions were geomagnetically quiet ($Kp = 1$). There was some substorm activity recorded earlier at 0700–1500 UT in ground magnetometer stations located around local midnight across Northern Canada (2000–0200 magnetic local time (MLT)). ACE data (not shown) indicate quiet solar wind conditions with $B_y \sim +4$ nT, $B_z \sim +2$ nT, $V_{sw} \sim 380$ km s^{-1} , and $P_{dyn} \sim 3$ nPa.

2.1. Ground-Based Optical and Radar Observations

Figure 1 shows a polar projection plot at 1608 UT of the ground-based instrumentation fields of view (FOVs) used in this study. The 80° and 70° AACGM (Altitude Adjustment Corrected Geomagnetic) [Baker and Wing, 1989] latitudes are marked on the plot along with longitudes at every 15° . The plot is orientated such that

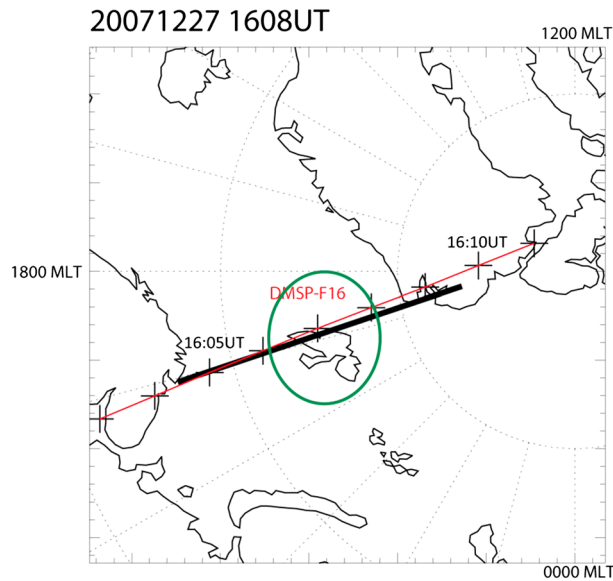


Figure 1. A polar projection plot of the ground-based instrumentation fields of view at 1608 UT along with the DMSP F16 satellite footprint (red line). The 80° and 70° AACGM latitudes are marked on the plot along with longitudes at every 15°. The field of view of the ASC 557.7 nm channel at an assumed altitude of 125 km (green circle) and the MSP (black line) are shown. Black crosses on the DMSP F16 track are set at 1 min cadence with 1605 and 1610 UT marked on.

1200 MLT is located at the top, 1800 MLT to the left, and 0000 MLT at the bottom. The black line indicates the FOV of the Longyearbyen Meridian Scanning Photometer (MSP). The instrument is located at 78.15°N, 16.02°E geographic (75.34°N, 111.1°E geomagnetic) in the Kjell Henriksen Observatory (KHO) and consists of a scanning mirror, scanning north to south in the geomagnetic meridian plane, narrow band tilting interference filters, and photo multiplier tubes. The data are recorded at an angular resolution of 1° and a temporal resolution of 16 s. The green circle shows the FOV for the 557.7 nm channel (utilizing a mapping altitude of 125 km) of the Interplanetary Space Physics Institute (IFSI-INAF) Ny Ålesund All-Sky Camera (ASC) which forms part of the MIRACLE network [Syrjasuo *et al.*, 1998]. The data have a temporal resolution of 20 s. The red line indicates the mapped footprint of the Defense Meteorological Satellite Program (DMSP) F16 satellite from 1603 to

1611 UT. The satellite is in a circular polar orbit at an altitude of 865 km. The black crosses are placed at a 1 min cadence. Data will also be presented from the EISCAT Svalbard Radar (ESR) 42 m dish, which is in a field-aligned position (81.6° elevation and 184.6° azimuth from geographic north). The ESR is collocated with the KHO but has a projected FOV on the order of approximately few kilometers at auroral emission altitudes and is thus not shown on the figure. It can be seen that the FOVs of the MSP and the DMSP F16 satellite are almost exactly aligned during this period, and thus, it is highly likely that DMSP F16 intersected with the ESR beam.

Figures 2a–2c present data from the ESR 42 m dish, from 1500 to 1730 UT (1800–2030 MLT). Figures 2a–2c show the electron density, ion temperature, and electron temperature between an altitude of 100 and 350 km at a temporal resolution of 30 s. The thick white vertical stripes at ~1540 UT and 1640 UT are data gaps due to the radar being in an airport interlock mode. Figures 2d and 2e present data from the MSP at (d) 630.0 nm and (e) 557.7 nm scanning along the geomagnetic meridian from a scan angle of 30°–150° (30° elevation north to 30° elevation south). The data are plotted out as a function of AACGM coordinates from 72 to 78° magnetic latitude (MLAT). An assumed emission altitude of 220 km and 125 km has been utilized for the mapping of the 630.0 nm and 557.7 nm observations, respectively, in line with modelling work of Johnsen and Lorentzen [2012]. The red horizontal dashed lines in Figures 2d and 2e indicate (from high to low latitude) the latitudinal position of Ny Ålesund (NYA), Longyearbyen (LYR), and Hornsund (HOR). The central horizontal red dashed line indicates also the field-aligned look direction (i.e., when the MSP observations were parallel to the ESR 42 m beam). The red vertical dashed line across all five panels indicates the time of the DMSP F16 satellite pass, data from which will be presented later. The MSP data set shows that between 1500 and 1730 UT 13 equatorward propagating arcs were observed. They are observed in both the 630.0 nm and 557.7 nm channels, corresponding to precipitating particle energies of <1 keV and 2–7 keV, respectively [del Pozo *et al.*, 2002, and references therein]. As expected at this MLT, the intensity of the green line emissions (557.7 nm) dominates over the red line emissions (630.0 nm). The optical intensity of the arcs is relatively low at ~2 kR in the case of the 630.0 nm emissions and ~5 kR in the case of the 557.7 nm emissions (at the limit of being visible to the naked eye). The full 180° FOV data (not shown) from the MSP show that arcs are indeed embedded within the auroral oval, the poleward edge of which is located at ~78° MLAT. This can

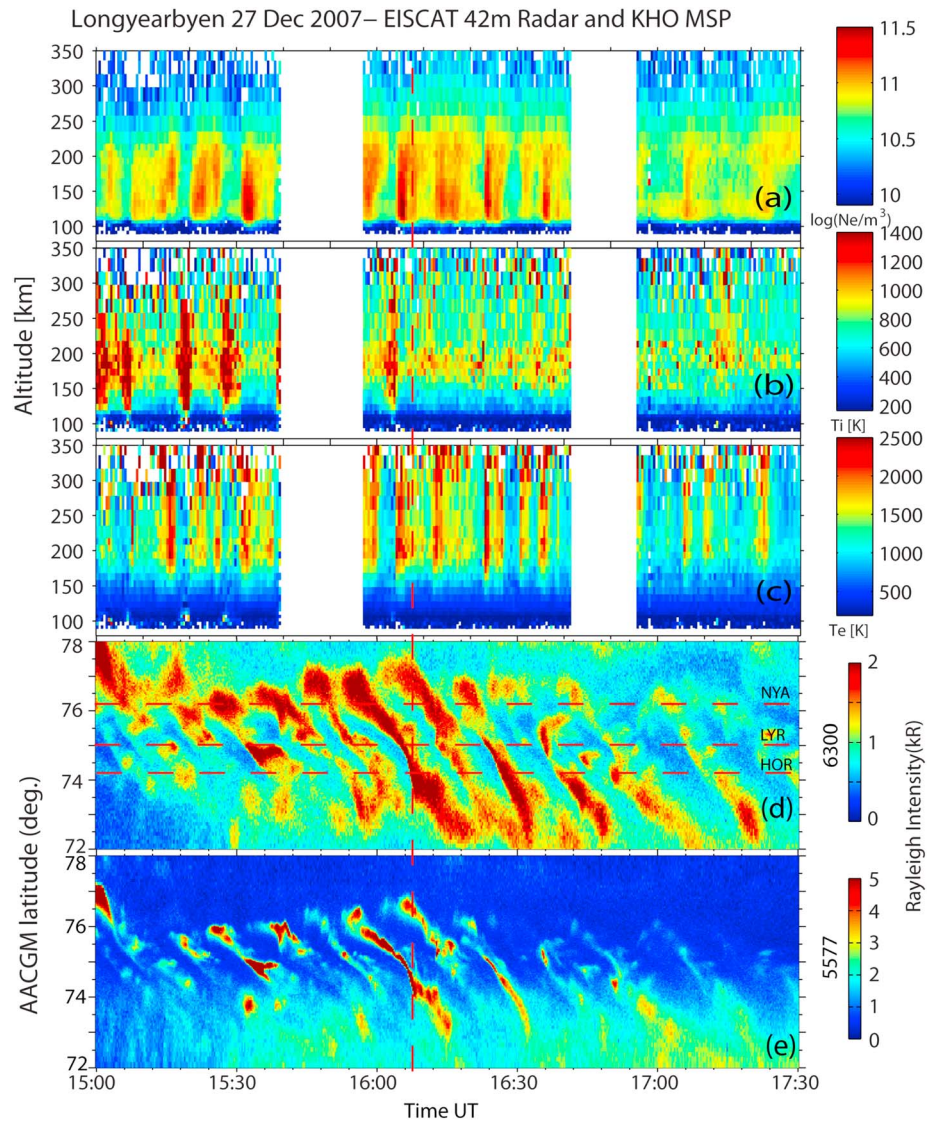


Figure 2. Ionospheric (a) electron density, (b) ion temperature, and (c) electron temperature measured by the EISCAT Svalbard radar 42 m dish as a function of altitude. Auroral intensities in the (d) 630.0 nm and (e) 557.7 nm wavelengths as measured by the meridian scanning photometer (MSP). The red horizontal dashed lines in Figure 2d mark the positions of NYA, LYR (also the pointing direction of the ESR 42 m beam on the MSP field of view), and HOR. The red vertical dashed line indicates the time of the DMSP F16 satellite conjunction.

be taken as a proxy for the open/closed field line boundary [Blanchard *et al.*, 1995], thus placing the wave activity on closed field lines. The arcs emanate from approximately 1° equatorward from the poleward edge of the oval at ~77° MLAT and propagate toward its equatorward edge at ~72° MLAT. There is distinct structure observed in each of the arcs, but an average equatorward propagation speed of ~0.46 km s⁻¹ was calculated, utilizing the assumed emission altitudes for each channel.

A close examination of Figures 2d and 2e indicates the large variability in the latitudinal width of the arcs as well as the distance between them as a function of time. Measurements of the full width half maximum of the emission peaks for the 557.7 nm channel of the MSP as each arc passes through zenith allowed estimates as to the latitudinal extent of the arcs. It was calculated that the arcs were ~10–15 km wide in latitudinal extent, comparable with previous observations [Samson *et al.*, 2003; Xu *et al.*, 1993; Mathews *et al.*, 2004]. At times when two arcs are observed in a single MSP scan period then the latitudinal distance between the arcs can be estimated. To minimize any ambiguities regarding mapping errors, calculations were performed only when both arcs were observed between scan angles of 60° and 120° (i.e., 30° in either side of zenith). The

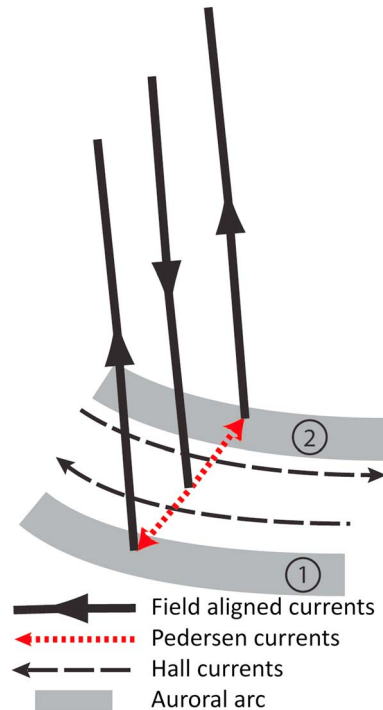


Figure 3. Schematic showing the ionospheric current systems induced by the ULF wavefield. North is at the top of the figure; thus, arc 2 is located poleward of arc 1. The arcs then progress equatorward with time with a total of 13 arcs being observed.

latitudinal distance between the arcs varied between 45 and 80 km. The latitudinal scale of the wavefield is thus of the order of 55–95 km.

From 1500 to 1730 UT the ESR observed distinctive periodic enhancements in all three EISCAT parameters shown. Electron density and electron temperature enhancements are observed during the periods where an arc propagates through the narrow field of view of the radar. Enhancements in both these parameters are indicative of energetic particle precipitation either through ionization processes or by thermal heating of the electrons. Electron density enhancements are observed between ~100 and 230 km altitude with the enhancements maximizing at ~130 km. The dominance of the 557.7 nm emissions, as observed in the MSP data, corroborates the peak ionization altitude (which is between 105 and 130 km for 2–7 keV electrons) [Rees, 1989] inferred from the electron density enhancements in the EISCAT data. The electron temperature enhancements

are observed at higher altitudes from ~130 to 250 km, maximizing at ~200 km. Ion temperature enhancements of up to 1700°K are observed adjacent to each of the arcs extending down to ~120 km, which are associated with Joule and/or ion frictional heating effects. The ion temperature enhancements indicate distinct small-scale ionospheric Pedersen current structures and electric fields between the arcs [e.g., *St. Maurice and Schunk, 1979*]. Figure 3 indicates a schematic of the proposed current flow (indicated by the arrows) into and surrounding the arcs (grey shaded regions), with arc 1 being located equatorward of arc 2 at a single moment in time (adapted from Figure 2 of *Samson et al. [2003]*). The FACs associated with the arcs are shown using the solid lines. The upward flowing FACs are associated with downward flowing electron flux. In between the arcs are downward flowing FAC regions. The Pedersen currents (indicated by a red dotted line) form the final part of the circuit allowing current closure in the ionosphere. The orientation of the current system is such that the associated ionospheric perpendicular electric field vector will be directed poleward on the equatorward side of the arc and equatorward on the poleward side of the arc. Such *E* field structures have been documented previously surrounding auroral arcs, [e.g., *Chaston, 2006*]. The resulting ionospheric Hall currents (indicated by a dashed line) are flowing in narrow channels between the arcs with an eastward (westward) direction on the poleward (equatorward) side of the arc.

Since the ionospheric flow vector is perpendicular to the magnetic field direction (and thus the pointing direction of the ESR beam), no corresponding velocity enhancements are seen by the ESR (data not shown). Ionospheric conditions at the time were also not conducive to HF radar backscatter techniques, such as those utilized by the Super Dual Auroral Radar Network (SuperDARN) radar systems [Greenwald et al., 1995]; hence, no direct measurements of the background ionospheric convection velocity over Svalbard are available.

An FFT analysis of multiple time series across MSP scan angles of between 60° and 120° in 10° intervals was undertaken. The time series data at each scan angle were band-pass filtered between 1 and 10 mHz. The resulting power spectra are shown in Figure 4 for both 557.7 nm (shown in green) and 630.0 nm (shown in red). The y axis on the left (right)-hand side of the plots shows the spectral power for the 557.7 nm (630.0 nm) channel and shows a dominant frequency of ~1.63 mHz (~615 s) placing the wave activity in the Pc5 category (the dominant frequency shifts by one data bin from 1.57 mHz to 1.69 mHz with

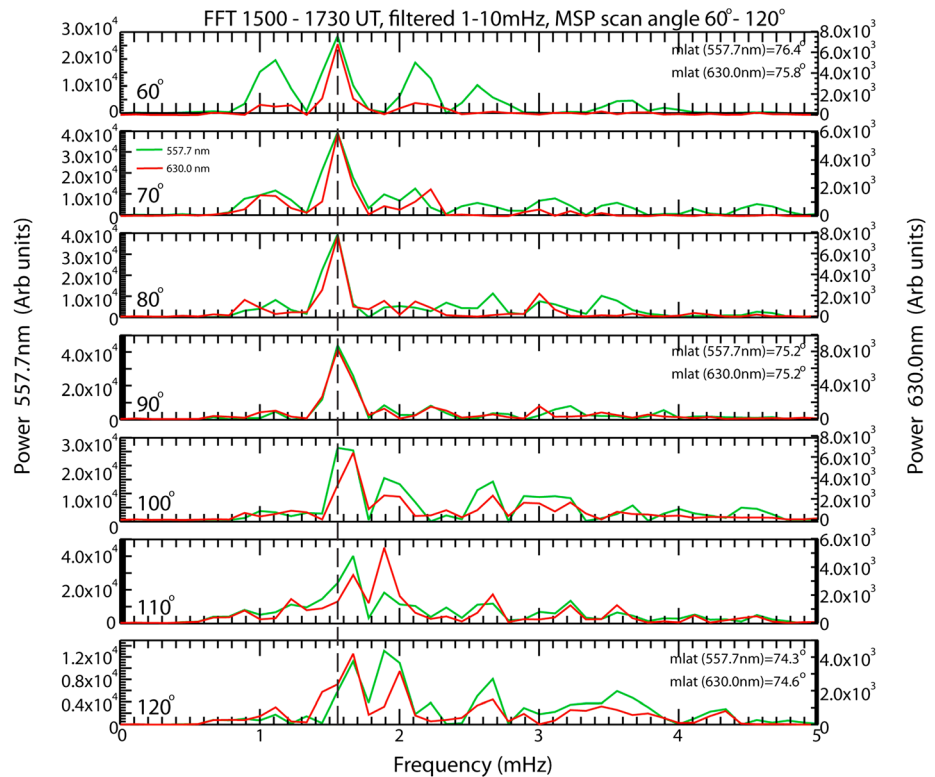


Figure 4. An FFT analysis of multiple time series taken from the MSP for a series of scan angles (60°–120°) for both 557.7 nm and 630.0 nm channels between 15.00 and 17.30 UT. The equivalent MLAT for both MSP channels is shown in the first, fourth, and seventh panels for the assumed emission heights. The data have been band-pass filtered between 1 and 10 mHz.

decreasing latitude). The MLAT which equates to the different scan angles for the different wavelength is shown on the right-hand side of the first, fourth, and seventh panels in Figure 4 (using the assumed emission altitudes mentioned earlier). The scan angle over which the analysis could be conducted covered only $\sim 2^\circ$ and $\sim 1^\circ$ in MLAT (for the 557.7 nm and 630.0 nm observations, respectively). When considered alongside the latitudinal extent of the entire wavefield (Figures 2d and 2e), this equates to observations across a single arc ($\sim 76^\circ$ – 74.3° MLAT). A latitudinal profile for both the phase and spectral power at 1.69 mHz for the 630.0 nm and 557.7 nm channels as a function of instrument scan angle (from 60° and 120°) and MLAT (not shown) confirms that the majority of the spectral power is confined into a very narrow region of less than 2° and peaking at $\sim 74.9^\circ$ MLAT. The magnitude of the phase difference across this single arc is $\sim 360^\circ$, greater than that expected for a single FLR. As shown in Figures 2d and 2e the wavefield across the entire oval consists of three parallel arc systems which would imply a phase change of $3 \times 360^\circ$. One possible explanation for this large apparent change of phase across the arcs is that phase differences are generating internal fine structuring inside a single FLR such as that described by Mann *et al.* [1995].

The MIRACLE ASC, located in Ny Ålesund (76.24°N , 110.19°E geomagnetic), was operational and provides information regarding the longitudinal structure of the wave. The 557.7 nm channel was utilized and the data mapped onto a geomagnetic grid at an assumed emission height of 125 km. Figure 5 shows an example of the data from 16:05 to 16:08 UT at 1 min cadence. Two arc structures are clearly visible in the image, extending over several degrees of longitude. Zenith in the ASC field of view is located at approximately, 60° (40°) scan angle on the 630.0 nm (557.7 nm) MSP data plot (Figures 2d and 2e). Comparing Figures 5 and 2d, it can be seen that the observations of the two arcs are consistent between both instruments. The three black squares indicate the position of NYA, LYR, and HOR. Throughout the time interval the arcs are observed to propagate from north east to south west across the ASC FOV. The westward propagation of the northern most arc can be clearly seen over the 3 min interval shown in Figure 5. Utilizing the method of Samson

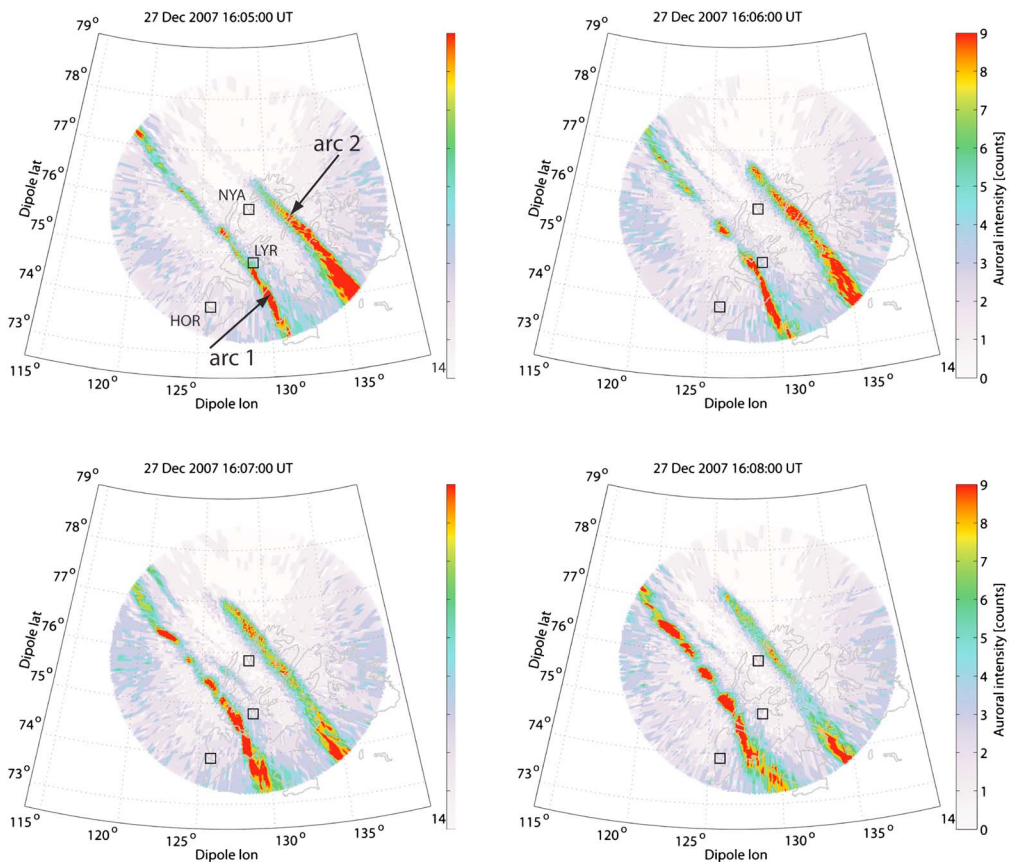


Figure 5. Data from the Ny Ålesund All-Sky Camera 557.7 nm channel at 1 min cadence from 1605 to 1608 UT, mapped onto dipolar coordinate system at an assumed altitude of 125 km. The intensity scale is in raw counts. Arcs 1 and 2 are marked on the top left. The three black squares indicate the position of Ny Ålesund (NYA), Longyearbyen (LYR), and Hornsund (HOR).

et al. [2003], the azimuthal velocity can be estimated. The method plots the maximum intensity (in latitude) of the arc as a function of longitude. The arc is then determined to be at the location of the maximum gradient. By observing the temporal motion of this gradient the propagation velocity can be calculated. While this method allows an estimation of the velocity, it does have its limitations. It relies on the intensity of one arc to be significantly larger than the other (or for only a single arc to be in the ASC field of view) to ensure that the observed maximum intensity gradient relates to the motion of a single arc. Additional fluctuations in auroral intensity and small-scale structuring within the arc can also make it difficult. A westward (azimuthal) propagation velocity of $\sim 0.04^\circ \text{ s}^{-1} \pm 0.01^\circ \text{ s}^{-1}$ ($\sim 1 \text{ km s}^{-1}$) was calculated. When considering the periodicity of the wave, this translates to an azimuthal m number of approximately -10 to -25 (the negative value indicating the westward propagation direction).

Unfortunately, as mentioned earlier, no direct measurement of the ionospheric convection velocity is available over Svalbard. However, velocities derived from the SuperDARN map potential model [Ruohoniemi and Baker, 1998], which take into account the prevailing Solar Wind conditions, indicate ionospheric velocities of $< 0.6 \text{ km s}^{-1}$. This would suggest that the auroral structures are not being simply convected with the background ionospheric flow (which would be in a sunward direction at these latitudes).

2.2. DMSP F16 Satellite Observations

Figure 6 shows data from the Special Sensor Ultraviolet Spectrographic Imager (SSUSI) onboard DMSP F16. The plot is part of a polar projection plot of the SSUSI imager data from the LBHS, 140–160 nm wavelength N_2 emissions [Germany *et al.*, 1997] from a single pass across the northern dusk polar region. The SSUSI sensor includes a line scanning imaging spectrograph which produces a horizon to horizon line scan (140° wide) at a temporal resolution of 22 s. The satellite was traversing the auroral oval, from dusk to dawn, and thus, the

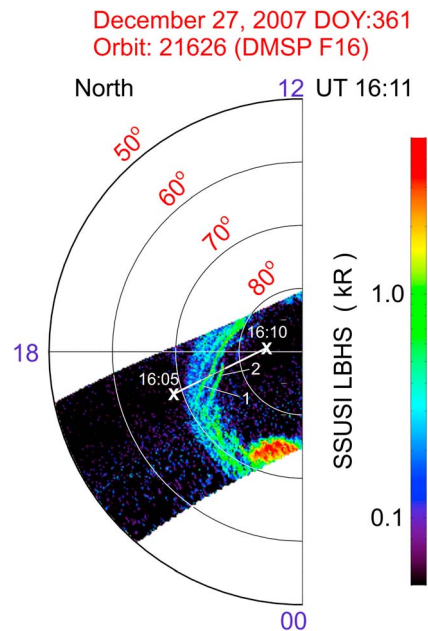


Figure 6. A polar projection plot from the DMSP F16 SSUSI instrument of auroral emissions in ultraviolet LBHS channel. AACGM latitudes are marked at 10° intervals from 80° to 50°. The 12, 18, and 00 MLT are also marked. The footprint of the satellite (projected down to ionospheric altitudes) is shown as a white line. The two white crosses mark the satellite location at 1605 and 1610 UT. Two arc structures, arcs 1 and 2, are also marked.

image in Figure 6 is composed of a times series of scans taken during one complete crossing of the oval (~ 15 min). The subsatellite track, geomagnetically mapped into the ionosphere, is marked by a white line. Time stamps are shown at 1605 UT and 1610 UT. Since DMSP F16 traverses the duskside oval region very rapidly in comparison to the wave period (~ 180 s compared to 600 s), then the observed structures can be considered as a “snapshot” of the wavefield, removing any spatiotemporal ambiguities. Three distinct parallel arcs are observed embedded within the main auroral oval on the duskside. They extend over several tens of degrees in longitude from ~17 to 21 MLT. Each arc extends poleward with decreasing MLT. The azimuthal scale size of the wave can also be observed in a more global context. The DMSP F16 data corroborate the ground-based MSP data in indicating that the structures are embedded within the main oval itself and thus on closed field lines. Auroral enhancements can also be seen

at ~23 MLT possibly associated with a small substorm. From ~1606 to 1608 UT the satellite passed across two of the arc structures (marked as 1 and 2 in Figure 6).

Figure 7 shows data from the DMSP F16 SSM (magnetometer) and the SSJ5 (electron and ion spectrometer) instruments [Hardy et al., 1984] from 1600 to 1610 UT. The spacecraft coordinates are also indicated along the x axis of the plot, and it is moving from low to high latitude in the dusk sector. The data for the SSM instrument have been rotated to a coordinate system aligned with the arcs with B_{par} in the direction parallel to the arc and B_{perp} in the direction perpendicular to the arc. Figure 7 shows the (a) delta-B_{perp} (black) and delta-B_{par} (red) magnetic field components, (b) electron differential energy flux, and (c) ion differential energy flux. Perturbations in the magnetic field components are indicative of FACs. The large fluctuations around 1601–1602 UT and 1607 UT are the result of a singularity in the calculation when the B field perturbation vector is aligned either parallel or antiparallel with the satellite direction vector (i.e., $\theta = \pm \frac{\pi}{2}$). Since the satellite is moving from equatorward to poleward on the dusk side, the large-scale Region 2 (R2) FAC is encountered before the large-scale Region 1 (R1) FAC. The extent of these large-scale currents is marked in Figure 7a. Focusing on the R1 current region, small magnetic perturbations can be observed embedded within this region, primarily in the B_{par} component, which indicates several small downward and upward current regions, marked by the red and blue arrows in Figure 7a. The black dashed vertical lines indicate when there is a reversal in the B field gradient. The direction of the currents is marked with red and blue arrows with a positive delta-B_{par} gradient indicating a downward current region and a negative delta-B_{par} gradient indicating an upward current region. Optical observations from the SSUSI instrument (shown in Figure 6) indicate that the arcs are extended current sheets, with a large longitudinal extension in comparison to their latitudinal extension. By applying Ampere’s law (and assuming a satellite velocity of ~7 km s⁻¹), perturbations in the magnetic field component parallel to the arcs (B_{par}) can be utilized to calculate the FAC density associated with the auroral structures when encountered by the satellite. Upward field-aligned current densities of ~0.5 μA m⁻² and ~0.8 μA m⁻² are calculated for arcs 1 and 2, respectively. Observations of FACs associated with larger-scale ULF wave structures, such as FLRs, have indicated larger current densities of ~10 μA m⁻² [e.g., Lotko et al., 1998; Walker et al., 1992].

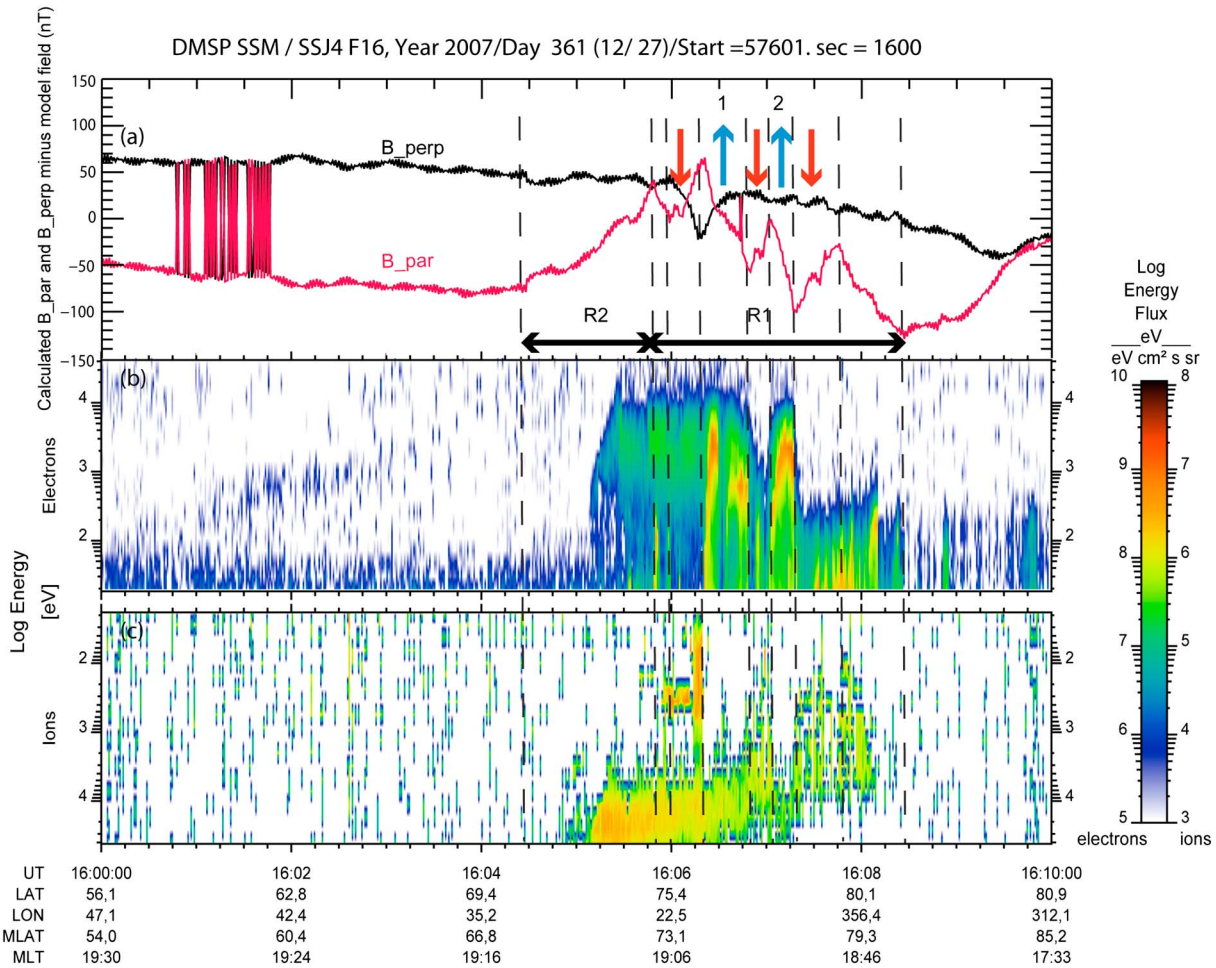


Figure 7. DMS F16 particle and magnetic field data from 1600 to 1610 UT. (a) Magnetic B_{perp} and B_{par} components. (b) Electron particle flux. (c) Ion particle flux. The large-scale R1 and R2 current systems are marked on. The red (blue) arrows indicate regions of downward (upward) currents associated with the auroral arcs embedded inside the large-scale R1 current system. Observation times corresponding to the two arcs (1 and 2) occurring at 16:06:30 and 16:05:00 are marked at the top of the figure.

The two upward current structures (1 and 2) are associated with a downward flowing population of energetic electrons. Figure 7b indicates the electron differential energy flux with electron energies inside the arcs of between 0.5 and 4.5 keV. The electron flux inside each of the arcs shows an inverted-V structure with the flux peaking between 1–4.5 keV in arc 1 and 0.5–3 keV in arc 2.

The vertical dashed red line in Figure 2 shows the approximate time that DMS F16 intersects with the FOV of the MSP and ESR beams. The equatorward to poleward trajectory of the spacecraft means that it will encounter the most equatorward arc first (arc 1 in Figure 6, located at approximately 74° MLAT) and then the poleward arc (arc 2 in Figure 6, located at approximately 77° MLAT). As seen in Figure 2e, the 557.7 nm emissions (indicative of precipitating particle energies of between 2 and 7 keV) are particularly dominant in arc 1 throughout the time it is observed by the MSP, at above 5 kR, which is in good agreement with the associated electron energies observed by DMS F16 of between 1.0 and 4.5 keV.

Inverted-V structures are indicative of electrons having passed through a U- or V-shaped potential structure (i.e., a region of parallel electric field, $E_{||}$), above the satellite location [Evans, 1974; Bosqued et al., 1986; Frey et al., 1998; Partamies et al., 2008]. The $E_{||}$ region is thought to extend for approximately $1 R_E$ above the F region ionosphere, and it is here in the auroral acceleration region that the electrons are accelerated up to the energies necessary to produce optical auroral signatures [e.g., Xu et al., 1993]. Several authors have indicated a link between ULF waves (in particular FLRs) and electron energization by an $E_{||}$, both through satellite [e.g., Chaston et al., 2002] and modelling work [e.g., Rankin et al., 2004]. Alternatively, Watt and Rankin [2009]

presented simulations of Alfvén wave acceleration of electrons from the plasma sheet into the ionosphere by considering the thermal velocity of the electrons in relation to the local Alfvén velocity along the geomagnetic field. They indicated that at altitudes above $\sim 4 R_E$ electrons can become trapped and accelerated by Alfvén waves. At altitudes below $\sim 4 R_E$, E_{\parallel} becomes sufficiently small that the electrons are no longer trapped and flow into the ionosphere, having being accelerated enough to produce auroral optical displays. These studies, in addition to others [e.g., Vaivads *et al.*, 2003; Wright *et al.*, 2003], have shown that a significant amount of the wave energy itself can be diverted into electron acceleration processes, representing an additional sink of wave energy in addition to ionospheric Joule heating effects. While the electron flux inside arc 2 has a single inverted-V structure, the one inside arc 1 has more structuring. From 16:06:15 to 16:06:30 there is an inverted-V population with electron energies ranging from 0.5 to 4.5 keV, while from 16:06:35 to 16:06:50 there appears to be a more monoenergetic population centered at ~ 0.5 keV. Examination of the B field data indicates that both populations are located within the same upward current region as observed by DMSP F16. Figures 6 and 2e also indicate additional internal structuring inside arc 1. While there are no significant electron fluxes associated with the downward FAC regions, there is a population of modestly accelerated ions located within the first downward current region. There is also a population hot (~ 10 keV) ions extending across the R2 and R1 current regions. The mean energy (decreasing with increasing latitude) and modest flux are consistent with field lines which map from the earthward edge of the current sheet further into the magnetotail. Concentrating on the upward FAC regions associated with arcs 1 and 2 and assuming an average electron energy of 1.5 keV, the downward electron energy flux inside the arcs is approximately 2.4 mW m^{-2} , similar to the larger-scale FLR event observed by Samson *et al.* [2003].

3. Discussion

3.1. Wave Characteristics and Energy Source

The relatively low frequency of the wave at this L shell ($L = 15$), (which is determined by the natural eigenfrequency of the field line [see, e.g., Orr and Hanson, 1981]) could be attributed to two things: sufficient mass loading of the field lines and the stretching of field lines toward the magnetotail. Both would reduce the eigenfrequency supported at this L shell. Mapping of field lines containing the auroral arcs from the ionosphere into the magnetospheric equatorial plane utilizing the TS01 model [Tsyganenko, 2002] and ACE Solar Wind data indicates that although the field lines are closed, there is significant field line stretching to distances of between ~ 20 and $25 R_E$ into the magnetotail. Field line stretching as an explanation for low-frequency FLRs has been inferred from both observations and models [e.g., Rankin *et al.*, 2005], and it is thus plausible that the low frequency of the pulsation presented here can be attributed to this.

The intermediate azimuthal scale size of the wave, in addition to its westward (and thus sunward) propagation at the observed MLT location, implies that the wave energy source is either related to energetic particle populations injected into the magnetosphere from the tail region or an interaction with a compressional mode wave with a sunward propagation direction. In the case of poloidal mode waves, the former is more favorable [e.g., Mager and Klimushkin, 2008; Baddeley *et al.*, 2004, and references therein], while in the case of toroidal mode waves the latter is more favorable [e.g., Glassmeier, 1995].

The structuring of toroidal and poloidal mode waves is such that any associated ground magnetic signature will be dominant in either the N (toroidal, local magnetic north-south) or E (poloidal, local magnetic east-west) component. In the case studies of poleward propagating auroral arcs presented by Samson *et al.* [2003] and Rankin *et al.* [2005] the wave signature was evident in the N component of colocated ground magnetometer data. This, coupled with this latitudinal profile and the low azimuthal m number, led to the conclusion that the waves were toroidal mode FLRs.

As mentioned earlier, the event occurred during geomagnetically quiet conditions. While there is evidence of substorm activity at lower latitudes several hours eastward in MLT from Longyearbyen, local geomagnetic conditions remained quiet both during and preceding the event ruling out a substorm generation mechanism such as that detailed in Rae *et al.* [2014]. An FFT analysis of the ground magnetometer data from the IMAGE chain [Gjerloev, 2012], detrended and band-pass filtered between 1 and 10 mHz, is shown in Figure 8 for both the N (red line) and E (blue line) components. The MSP observations in Figure 2 show the arcs extend from $\sim 77^\circ$ to 72° MLAT. The ground magnetometer data from the four stations (NYA, LYR, HOR, and BJN) extend from 76.3° to 71.5° MLAT (as shown on the right-hand side of Figure 8). There is

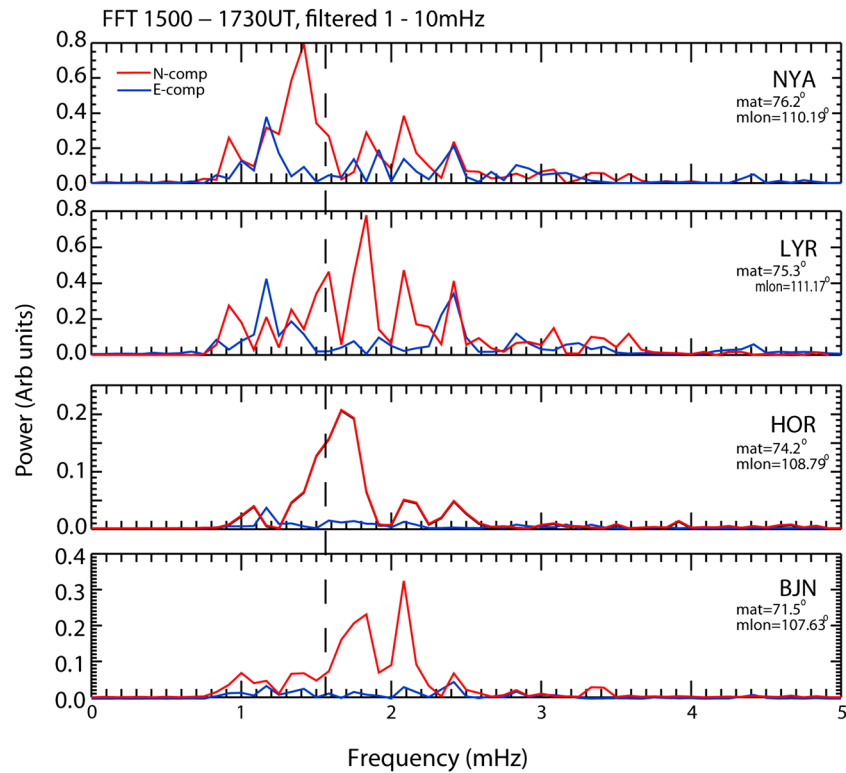


Figure 8. An FFT analysis of ground magnetometer data from NYA, LYR, HOR, and BJN for 15.00–17.30 UT. The data were linearly detrended before being band-pass filtered between 1 and 10 mHz. Data are shown for both the north-south (*N*) and east-west (*E*) components.

wave activity observed within the Pc5 range in the *N* component across all four stations; however, in the case of NYA and LYR (which lie directly beneath the arcs) there are multiple spectral peaks with the dominant spectral peak not at the same frequency as that observed in the MSP data. An examination of the filtered magnetometer time series data indicated wave activity at 1.69 mHz primarily from 16.20 to 17.30 UT at HOR, located toward the equatorward edge of the oval, with a peak to peak value of ~10 nT. This lack of apparent ground signature could be due to a combination of two factors. First, the magnitude of the current systems associated with the arcs is very small (as is demonstrated by the low magnitude FAC and particle fluxes) making any ground magnetic response difficult to detect. Second, the scale size of the ULF wave itself makes it possible to “screen” it from ground magnetometers. It is a well-documented phenomenon [e.g., Hughes and Southwood, 1976; Yeoman et al., 2008; Baddeley et al., 2005] associated with small-scale ULF waves and is related to the spatial integration imposed upon ground magnetometers and the attenuation of the magnetic signature between the ionosphere and the ground. Following the analysis of Hughes and Southwood [1976], when considering the screening of ionospheric current systems generated by ULF waves from the ground, the perpendicular scale size, k_{\perp} , of the wave with respect to the background magnetic field is the dominant factor, where

$$k_{\perp} = (k_{\text{mer}}^2 + k_{\text{az}}^2)^{0.5} \quad (1)$$

and k_{mer} is the meridional *k* vector and k_{az} is the azimuthal *k* vector. The amount of screening, *s*, can be estimated as

$$s \sim \exp(-k_{\perp}h) \quad (2)$$

where *h* is the height of the ionospheric *E* region (~100 km). For the wave event presented here $k_{\text{mer}} \sim 2\pi/110$ and $k_{\text{az}} \sim 2\pi/483$ (where 483 km is the distance at 75° MLAT of one wavelength). Using equations (1) and (2) would result in a screening factor, *s*, of 0.0025. Applying this to the magnetic field perturbations observed by DMSP as it crossed the wavefield ($\Delta b_{\perp, \text{av}} \sim 120$ nT) implies a corresponding ground signature of < 1 nT. Such

a signature would be very difficult to isolate from the general random small-scale fluctuations in the magnetic field. However, since the majority of wave activity shown in Figure 8 is observed in the N component, then this is suggestive of a primarily toroidal structure pulsation but the lack of a dominant signature at ~ 1.63 mHz beneath the arcs from 15.00 to 16.20 UT (in the case of HOR) and for the entire interval (in the case of NYA and LYR) makes a definitive conclusion challenging.

As mentioned earlier, the event presented in this paper shares several similarities to the event presented by *Mathews et al.* [2004]: both were observed over Svalbard at the same MLT and had a similar frequency and an equatorward and sunward propagation direction. The events differ, however, in their propagation speeds with the *Mathews et al.* [2004] event having an equatorward propagation speed of $1.3^\circ \text{ min}^{-1}$ and an azimuthal propagation speed of 2.2 km s^{-1} (in comparison to $1.3^\circ \text{ min}^{-1}$ and 1 km s^{-1} , respectively, in the event presented here). In their event they suggested that the stretching of the field lines tailward in the flanks combined with an earthward propagating fast mode driver would account for the propagation directions. In the magnetospheric equatorial plane the parallel phase fronts of the earthward propagating fast mode would encounter field lines which map to a higher magnetic latitude first (i.e., the most poleward). Due to the field line stretching, the propagation time from the equatorial plane to the ionosphere would be sufficient to overcome the time taken for the fast mode wave to impinge upon the corresponding lower latitude field line. As such any effects observed in the ionosphere (such as the resulting auroral arcs) would appear to have an equatorward propagation. Applying the simple model suggested by *Mathews et al.* [2004] (cf. equations (1)–(6) in their paper) to this event here would require an alpha value of $\alpha \sim 0.2$ ($\alpha = v_{\text{gf}}/v_{\text{gA}}$, where v_{gf} is the fast mode equatorial group speed and v_{gA} is the equatorial Alfvén speed). It is thus entirely plausible that such a generation mechanism could explain the event presented here.

The large change of phase across the latitudinal extent of the wavefield is also suggestive of phase mixing occurring inside the FLR, generating multiple smaller-scale arcs. As discussed in *Mann et al.* [1995] such fine-scale structuring can occur with an energy source in the form of a damped compressional mode wave which in this case would require a sunward propagation direction.

3.2. Energy Dissipation in the Ionosphere

The simple model of a standing wave structure along a magnetic field line assumes infinite ionospheric conductivity, resulting in a perfectly reflecting ionospheric layer. However, a finite conductivity, as is the actual case, results in the wave energy being dissipated into the ionosphere, through Joule and/or ion frictional heating. As such, enhancements of Σ_p can be indications of the wave damping processes in the ionosphere. In the case where the ULF wave is associated with auroral modulation then there will be an additional contribution to any observed conductivity enhancements in the form of energetic particle precipitation.

ESR measurements of the ionospheric electron densities and temperatures can be combined with atmospheric parameters (neutral temperatures and densities) from the NRLMSISE-00 Model [*Picone et al.*, 2002], to estimate the height-integrated ionospheric Pedersen conductivity, Σ_p . The large electron density inside the arcs results in average Σ_p enhancements of between 5 and 10 S (although the enhancements in arc 1 reached $\Sigma_p \sim 17$ S). Outside the arcs the average Σ_p was lower at ~ 3 S. The magnitude of the background conductivity was discussed by *Rankin et al.* [2004], who noted that for the wave amplitude to increase to sufficient levels, the background ionospheric conductivity should be sufficient (> 0.5 S) to allow the ionospheric layer to be partially reflective. This in turn allows the wavefield, and associated FACs, to increase to a point where the ionospheric conductivity is modified by the wavefield itself and the FLR amplitude grows. Following the work of *Hughes* [1983], equation (3) shows the height-integrated form of Ampere's law (neglecting the displacement and ion polarization currents)

$$\Delta b_{\perp} = \mu_0 E_{\perp} \int_{z_0}^{z_0+z} \sigma_p dz = \mu_0 \Sigma_p E_{\perp} \quad (3)$$

where Δb_{\perp} and ΔE_{\perp} are the magnetic and electric field perturbations associated with the Alfvén wave, Σ_p is the height-integrated Pedersen conductivity, and dz the ionospheric altitude range.

Applying the DMSP F16 magnetometer data, the corresponding perpendicular electric field values, ΔE_{\perp} of $\sim 7 \text{ mV m}^{-1}$ and $\sim 12 \text{ mV m}^{-1}$, are obtained for arcs 1 and 2 ($\Delta b_{\perp} \sim 130 \text{ nT}$ and $\sim 112 \text{ nT}$, respectively). The resulting downward Poynting flux, as measured at DMSP, inside each arc is estimated to be $\sim 0.7 \text{ mW m}^{-2}$ and $\sim 1.1 \text{ mW m}^{-2}$, respectively. Since the electron acceleration process has occurred at an altitude above

the spacecraft, then this Poynting flux should be taken as a minimum value. In the paper presented here the particle energy flux inside each arc (estimated from DMSP F16 particle data) is $\sim 2.4 \text{ mW m}^{-2}$, which is approximately 2–3.5 times larger than the minimum Poynting flux. Conversely, in between the arcs where conductivities are lower, the electric fields are larger, giving rise to a larger Poynting flux. This is also reflected in the larger ionospheric ion temperatures observed in between the arcs in comparison to inside the arcs, since ion temperature is proportional to the electric field value squared [e.g., *St. Maurice and Schunk*, 1979]. Ion temperatures of $\sim 1700 \text{ K}$ equate to electric field values of $\sim 30 \text{ mV m}^{-1}$. This approximation should be treated as an order of magnitude estimate, utilizes a modelled ionospheric composition, and also assumes that the measured ion velocity is equivalent to the relative velocity between the ions and the neutrals. However, this value is consistent with the corresponding magnetic field perturbations in between the arcs as measured by DMSP F16. Outside the arcs, the particle flux energy is negligible (which is reflected in the lack of ionospheric electron density enhancements observed by the ESR). This anticorrelation between ionospheric ion temperature enhancements and electron density enhancements associated with auroral arcs has been previously shown to act as an indicator of the interplay between the Poynting flux and particle energy flux [e.g., *Thayer and Semeter*, 2004]. From *Wright et al.* [2003, equation (5)], the expected ratio between the electron energy flux density and the Poynting vector associated with ULF waves can be estimated using the ionospheric conductivity, electron velocity, and the latitudinal wavelength of the wave. They indicated that for a fully phase mixed FLR with a latitudinal wavelength of 25 km, the energization of electrons associated with the auroral arcs represents an energy sink for the wavefield which was 3 times greater than that of Joule heating. This is in line with the observations presented here.

4. Conclusions

We have presented a multiinstrument study of equatorward propagating auroral arcs driven by a standing mode Alfvén wave in the dusk sector ionosphere. The unique data set allowed direct measurements of the precipitating particle populations inside the arcs and ionospheric ion temperature enhancements in between the arcs. While the magnitude of the FACs is smaller than those carried by traditional FLRs ($< 1 \mu\text{A m}^{-2}$ in comparison to $10 \mu\text{A m}^{-2}$), the particle energies are still sufficient to induce auroral emissions at both 557.7 and 630.0 nm. Observations indicated that significant energy was lost from the wavefield due to both ionospheric Joule and/or ion frictional heating and also through electron acceleration by means of a parallel electric field in line with that predicted by models. The latitudinal phase structure of the 1.63 mHz wave, as deduced by the MSP, across a single arc, indicated a large ($\sim 360^\circ$) change of phase. When considering the wavefield that consisted of three parallel arcs, this suggests phase mixing generating internal fine structuring within a FLR. Due to ionospheric attenuation, no direct magnetic signature of the wave was detected on the ground; however, there was an increase in wave activity between 1 and 2.5 mHz in the north-south component, which is consistent with FLR activity. In addition to the equatorward phase propagation the event had a sunward propagation direction and medium azimuthal scale size ($m \sim |10|$ – $|25|$) leading to the conclusion that the energy source is internal to the Earth's magnetosphere, most likely in the form of a compressional mode wave emanating from the magnetotail with an earthward propagation. In future, this data set could prove very useful to the modelling community concerning the nature of auroral arcs driven by ULF waves with an energy source internal to the magnetosphere.

References

- Baddeley, L. J., T. K. Yeoman, D. M. Wright, K. J. Trattner, and B. J. Kellet (2004), Statistical study of unstable particle populations in the global ring current and their relation to the generation of high m ULF waves, *Ann. Geophys.*, 22, 4229–4241, doi:10.5194/angeo-22-4229-2004.
- Baddeley, L. J., T. K. Yeoman, and D. M. Wright (2005), HF doppler sounder measurements of the ionospheric signatures of small scale ULF waves, *Ann. Geophys.*, 23, 1807–1820, doi:10.5194/angeo-23-1807-2005.
- Baker, K. B., and S. Wing (1989), A new magnetic coordinate system for conjugate studies at high latitudes, *J. Geophys. Res.*, 94(A7), 9139–9143, doi:10.1029/JA094iA07p09139.
- Blanchard, G. T., L. R. Lyons, J. C. Samson, and F. J. Rich (1995), Locating the polar cap boundary from observations of 6300 Å auroral emission, *J. Geophys. Res.*, 100(A5), 7855–7862, doi:10.1029/94JA02631.
- Bosqued, J. M., C. Maurel, J. A. Sauvaud, R. A. Kovrazhkin, and Y. I. Galperin (1986), Observations of auroral electron inverted-V structures by the AUREOL-3 satellite, *Planet. Space Sci.*, 34(3), 255–269.
- Chaston, C. C., J. W. Bonnell, L. M. Peticolas, C. W. Carlson, J. P. McFadden, and R. E. Ergun (2002), Driven Alfvén waves and electron acceleration: A fast case study, *Geophys. Res. Lett.*, 29(11), 1535, doi:10.1029/2001GL013842.
- Chaston, C. C. (2006), ULF waves and auroral electrons, in *Magnetospheric ULF Waves: Synthesis and New Directions*, edited by K. Takahashi et al., p. 239, AGU, Washington, D. C.

Acknowledgments

This research was partly funded by the Research Council of Norway (project 246725 and contract 223252/F50). The Longyearbyen MSP is owned and operated by the University Centre in Svalbard and partly funded by the Research Council of Norway (project 195385). The MSP data can be obtained from Dag Lorentzen (e-mail: dagl@unis.no). The EISCAT scientific association is supported by the research organizations of Norway (NFR), Sweden (VR), Finland (SA), Japan (NIPR and STEL), China (CRIRP), and the United Kingdom (NERC). Data from EISCAT can be obtained from the Madrigal database <http://www.eiscat.se/madrigal>. The MIRACLE network is operated as an international collaboration under the leadership of the Finnish Meteorological Institute (FMI). IFSI-INAF (Italy) maintains the ITACA ASC in Ny Ålesund, and the ASC data can be obtained from Noora Partimies (noora.partimies@unis.no). We thank Liisa Juusola (FMI) for the dipole field projection of ASC images. The DMSP F16 particle and magnetic field data can be obtained from William Denig (e-mail: william.denig@noaa.gov). The DMSP F16 SSUSI data can be downloaded from the SSUSI website (<http://ssusi.jhuapl.edu/>). IMF and solar wind data are available at the NASA OMNIWeb service (<http://omniweb.gsfc.nasa.gov>). For the ground magnetometer data we gratefully acknowledge Eija Tanskanen (FMI).

- Chen, L., and A. Hasegawa (1991), Kinetic theory of geomagnetic pulsations, 1, Internal excitations by energetic particles, *J. Geophys. Res.*, *96*(A2), 1503–1512, doi:10.1029/90JA02346.
- Chisham, G., I. R. Mann, and D. Orr (1997), A statistical study of giant pulsation latitudinal polarization and amplitude variation, *J. Geophys. Res.*, *102*(A5), 9619–9629, doi:10.1029/97JA00325.
- del Pozo, C. F., M. J. Kosch, and F. Honary (2002), Estimation of the characteristic energy of electron precipitation, *Ann. Geophys.*, *20*, 1349–1359, doi:10.5194/angeo-20-1349-2002.
- Evans, D. S. (1974), Precipitating electron fluxes formed by a magnetic field aligned potential difference, *J. Geophys. Res.*, *79*(19), 2853–2858, doi:10.1029/JA079i019p02853.
- Frey, H. U., G. Haerendel, J. H. Clemmons, M. H. Boehm, J. Vogt, O. H. Bauer, D. D. Wallis, L. Blomberg, and H. Lühr (1998), Freja and ground-based analysis of inverted-V events, *J. Geophys. Res.*, *103*(A3), 4303–4314, doi:10.1029/97JA02259.
- Germany, G. A., G. K. Parks, M. Brittnacher, J. Cumnock, D. Lummerzheim, J. F. Spann, L. Chen, P. G. Richards, and F. J. Rich (1997), Remote determination of auroral energy characteristics during substorm activity, *Geophys. Res. Lett.*, *24*, 995–998, doi:10.1029/97GL00864.
- Gjerloev, J. W. (2012), The SuperMAG data processing technique, *J. Geophys. Res.*, *117*, A09213, doi:10.1029/2012JA017683.
- Glassmeier, K.-H. (1995), ULF pulsations, in *Handbook of Atmospheric Electrodynamics*, edited by H. Holland, pp. 463–502, CRC Press, Boca Raton, Fla.
- Greenwald, R. A., et al. (1995), DARN/superDARN, *Space Sci. Rev.*, *71*(1–4), 761–796.
- Hardy, D. A., L. K. Schmitt, M. S. Gussenhoven, F. J. Marshall, H. C. Yeh, T. L. Shumaker, A. Hube, and J. Pantazis (1984), Precipitating electron and ion detectors (SSJ/4) for the block 5D/flights 6–10 DMSP satellites: Calibration and data presentation, *Tech. Rep. AFGL-TR-84-0317*, Air Force Geophys. Lab., Hanscom Air Force Base, Mass.
- Hughes, W. J. (1983), Hydromagnetic waves in the magnetosphere, in *Solar Terrestrial Physics*, edited by R. L. Carovillano and J. M. Forbes, D. Reidel, Dordrecht, Netherlands.
- Hughes, W. J., and D. J. Southwood (1976), The screening of micropulsations by the atmosphere and ionosphere, *J. Geophys. Res.*, *81*(19), 3234–3240, doi:10.1029/JA081i019p03234.
- Johnsen, M. G., and D. A. Lorentzen (2012), The dayside open/closed field line boundary as seen from space- and ground-based instrumentation, *J. Geophys. Res.*, *117*, A03320, doi:10.1029/2011JA016983.
- Lotko, W., A. V. Streltsov, and C. W. Carlson (1998), Discrete auroral arc, electrostatic shock and suprathermal electrons powered by dispersive, anomalously resistive field line resonance, *Geophys. Res. Lett.*, *25*, 4449–4452, doi:10.1029/1998GL900200.
- Mager, P. N., and D. Y. Klimushkin (2008), Alfvén ship waves: High m ULF pulsations in the magnetosphere generated by a moving plasma inhomogeneity, *Ann. Geophys.*, *26*, 1653–1663, doi:10.5194/angeo-26-1653-2008.
- Mann, I. R., and A. N. Wright (1999), Diagnosing the Excitation Mechanisms of Pc5 Magnetospheric Flank Waveguide Modes and FLRs, *Geophys. Res. Lett.*, *26*, 16, doi:10.1029/1999GL900573.
- Mann, I. R., A. N. Wright, and P. S. Cally (1995), Coupling of magnetospheric cavity modes to field line resonances: A study of resonance widths, *J. Geophys. Res.*, *100*(A10), 19,441–19,456, doi:10.1029/95JA00820.
- Mathews, J. T., I. R. Mann, I. J. Rae, and J. Moen (2004), Multi-instrument observations of ULF wave-driven discrete auroral arcs propagating sunward and equatorward from the poleward boundary of the duskside auroral oval, the duskside auroral oval, *Phys. Plasmas*, *11*, 1250–1259, doi:10.1063/1.1647137.
- Newton, R. S., D. J. Southwood, and W. J. Hughes (1978), Damping of geomagnetic pulsations by the ionosphere, *Planet. Space Sci.*, *26*, 201–209, doi:10.1016/0032-0633(78)90085-5.
- Orr, D., and H. W. Hanson (1981), Geomagnetic pulsation phase patterns over an extended latitude array, *J. Atmos. Terr. Phys.*, *43*, 899–910, doi:10.1016/0021-9169(81)90081-7.
- Partamies, N., E. Donovan, and D. Knudsen (2008), Statistical study of inverted-V structures in FAST data, *Ann. Geophys.*, *26*, 1439–1449, doi:10.5194/angeo-26-1439-2008.
- Picone, J. M., A. E. Hedin, D. P. Drob, and A. C. Aikin (2002), NRLMISE-00 empirical model of the atmosphere: Statistical comparisons and scientific issues, *J. Geophys. Res.*, *107*(A12), 1468, doi:10.1029/2002JA009430.
- Rae, I. J., et al. (2005), Evolution and characteristics of global Pc5 ULF waves during a high solar wind speed interval, *J. Geophys. Res.*, *110*, A12211, doi:10.1029/2005JA011007.
- Rae, I. J., K. R. Murphy, C. E. J. Watt, G. Rostoker, R. Rankin, I. R. Mann, C. R. Hodgson, H. U. Frey, A. W. Degeling, and C. Forsyth (2014), Field line resonances as a trigger and a tracer for substorm onset, *J. Geophys. Res. Space Physics*, *119*, 5343–5363, doi:10.1002/2013JA018889.
- Rankin, R., J. Y. Lu, R. Marchand, and E. F. Donovan (2004), Spatiotemporal characteristics of ultra-low frequency dispersive scale shear Alfvén waves in the Earth's magnetosphere, *Phys. Plasmas*, *11*(4), 1268–1276, doi:10.1063/1.1647138.
- Rankin, R., K. Kabin, J. Y. Lu, I. R. Mann, R. Marchand, I. J. Rae, V. T. Tikhonchuk, and E. F. Donovan (2005), Magnetospheric field-line resonances: Ground-based observations and modeling, *J. Geophys. Res.*, *110*, A10S09, doi:10.1029/2004JA010919.
- Rees, M. H. (1989), *Physics and Chemistry of the Upper Atmosphere*, *Cambridge Atmos. Space Sci. Ser.*, Cambridge Univ. Press, Cambridge, U. K.
- Ruohoniemi, J. M., and K. B. Baker (1998), Large-scale imaging of high-latitude convection with Super Dual Auroral Radar Network HF radar observations, *J. Geophys. Res.*, *103*(A9), 20,797–20,811, doi:10.1029/98JA01288.
- Samson, J. C., L. L. Cogger, and Q. Pao (1996), Observations of field line resonances, auroral arcs, and auroral vortex structures, *J. Geophys. Res.*, *101*, 17,373–17,383, doi:10.1029/96JA01086.
- Samson, J. C., R. Rankin, and V. T. Tikhonchuk (2003), Optical signatures of auroral arcs produced by field line resonances: Comparison with satellite observations and modeling, *Ann. Geophys.*, *21*, 933–945, doi:10.5194/angeo-21-933-2003.
- Southwood, D. J., and W. J. Hughes (1983), Theory of hydromagnetic waves in the magnetosphere, *Space Sci. Rev.*, *35*(4), 301–366, doi:10.1007/BF00169231.
- St. Maurice, J. P., and R. W. Schunk (1979), Ion velocity distributions in the high-latitude ionosphere, *Rev. Geophys. Space Phys.*, *17*, 99–134.
- Syrjasuo, M. T., et al. (1998), Observations of substorm electrodynamics using the MIRACLE network, in *Substorms-4*, edited by S. Kokubun and Y. Kamide, pp. 111–114, Terra Sci., Tokyo.
- Thayer, J. P., and J. Semeter (2004), The convergence of magnetospheric energy flux in the polar atmosphere, *J. Atmos. Sol. Terr. Phys.*, *66*, 807–824, doi:10.1016/j.jastp.2004.01.035.
- Tsyganenko, N. A. (2002), A model of the near magnetosphere with a dawn-dusk asymmetry: 1. Mathematical structure, *J. Geophys. Res.*, *107*(A8), 1179, doi:10.1029/2001JA000219.
- Vaivads, A., et al. (2003), What high altitude observations tell us about the auroral acceleration: A Cluster/DMSP conjunction, *Geophys. Res. Lett.*, *30*(3), 1106, doi:10.1029/2002GL016006.
- Walker, A. D. M., R. A. Greenwald, W. F. Stuart, and C. A. Green (1979), STARE auroral radar observations of Pc 5 geomagnetic pulsations, *J. Geophys. Res.*, *84*, 3373–3388, doi:10.1029/JA084iA07p03373.

- Walker, A. D. M., J. M. Ruohoniemi, K. B. Baker, R. A. Greenwald, and J. C. Samson (1992), Spatial and temporal behavior of ULF pulsations observed by the Goose Bay HF Radar, *J. Geophys. Res.*, *97*(A8), 12,187–12,202, doi:10.1029/92JA00329.
- Watt, C. E. J., and R. Rankin (2009), Electron trapping in shear Alfvén waves that power the aurora, *Phys. Rev. Lett.*, *102*, 045002, doi:10.1103/PhysRevLett.102.045002.
- Wright, A. N., and I. R. Mann (2006), Global MHD Eigenmodes of the outer magnetosphere, in *Magnetospheric ULF Waves, Synthesis and New Directions*, *Geophys. Monogr. Ser.*, edited by K. Takahashi et al., vol. 169, pp. 51–72, AGU, Washington, D. C., doi:10.1029/169GM06.
- Wright, A. N., W. Allan, and P. A. Damiano (2003), Alfvén wave dissipation via electron energization, *Geophys. Res. Lett.*, *30*(16), 1847, doi:10.1029/2003GL017605.
- Xu, B.-L., J. C. Samson, W. W. Liu, F. Creutzberg, and T. J. Hughes (1993), Observations of optical aurora modulated by resonant Alfvén waves, *J. Geophys. Res.*, *98*(A7), 11,531–11,541, doi:10.1029/93JA00435.
- Yeoman, T. K., L. J. Baddeley, R. S. Dhillon, T. R. Robinson, and D. M. Wright (2008), Bistatic observations of large and small scale ULF waves in SPEAR-induced HF coherent backscatter, *Ann. Geophys.*, *26*, 2253–2263, doi:10.5194/angeo-26-2253-2008.
- Zheng, Y., et al. (2006), Coordinated observation of field line resonance in the mid-tail, *Ann. Geophys.*, *24*, 707–723, doi:10.5194/angeo-24-707-2006.